

Oxygen isotopic ratios in first dredge-up red giant stars and nuclear reaction rate uncertainties revisited

Jeffrey A. Stoesz^{1,2} and Falk Herwig^{1*}

¹*Physics and Astronomy Department, University of Victoria, Canada*

²*Herzberg Institute for Astrophysics, National Research Council, Victoria, Canada*

Submitted Sept 2002

ABSTRACT

We describe a general yet simple method to analyse the propagation of nuclear reaction rate uncertainties in a stellar nucleosynthesis and mixing context. The method combines post-processing nucleosynthesis and mixing calculations with a Monte Carlo scheme. With this approach we reanalyze the dependence of theoretical oxygen isotopic ratio predictions in first dredge-up red giant branch stars in a systematic way. Such predictions are important to the interpretation of pre-solar Al_2O_3 grains from meteorites. The reaction rates with uncertainties were taken from the NACRE compilation (Angulo et al. 1999). We include seven reaction rates in our systematic analysis of stellar models with initial masses from 1 to 3 M_\odot . We find that the uncertainty of the reaction rate for reaction $^{18}\text{O}(p, \alpha)^{15}\text{N}$ typically causes an error in the theoretical $^{16}\text{O}/^{18}\text{O}$ ratio of $\simeq +20/-5$ per cent. The error of the $^{16}\text{O}/^{17}\text{O}$ prediction is 10–40 per cent depending on the stellar mass, and is persistently dominated by the comparatively small uncertainty of the $^{16}\text{O}(p, \gamma)^{17}\text{F}$ reaction. With the new estimates on reaction rate uncertainties by the NACRE compilation, the p-capture reactions $^{17}\text{O}(p, \alpha)^{14}\text{N}$ and $^{17}\text{O}(p, \gamma)^{18}\text{F}$ have virtually no impact on theoretical predictions for stellar mass $\leq 1.5 M_\odot$. However, the uncertainty in $^{17}\text{O}(p, \alpha)^{14}\text{N}$ has an effect comparable to or greater than that of $^{16}\text{O}(p, \gamma)^{17}\text{F}$ for masses $> 1.5 M_\odot$, where core mixing and subsequent envelope mixing interact. In these cases where core mixing complicates post-dredge-up surface abundances, uncertainty in other reactions have a secondary but noticeable effect on surface abundances.

Key words: abundances – stars, nucleosynthesis

1 INTRODUCTION

Observations of abundances and abundance ratios in stars yield powerful constraints on models of internal processes in stars. In particular, the predicted abundance evolution of stars of a given mass and metallicity depends on both mixing and nuclear burning processes. While it is customary to provide observational results with some estimate or analysis of the associated errors, this is seldomly done for theoretical abundance predictions. This is partly due to the fact that quantitative uncertainties on the input physics is not available and that theoretical model uncertainties (in particular for poorly understood mixing processes) are hard to make. Finally, a systematic error propagation in stellar models can be computationally demanding and the effort has often not been justified in the past. However, new spectroscopic observations with unprecedented precision will be available in the near future, and one has the impression that stellar physics in general is entering a new high-precision era. In this context it seems necessary to reconsider the question of abundance prediction uncertainties in a quantitative way.

As an initial step in this direction, we have chosen specifically the dependence of oxygen isotopic ratio predictions in giant stars on nuclear reaction rate uncertainties. The oxygen isotopic ratios are of particular interest because they are affected not only by nucleosynthesis but also by mixing processes which are not yet very well understood. The latter is evident from the spectroscopic properties of giant stars which are not entirely consistent with standard stellar evolution models (Harris, Lambert, & Smith 1985; Harris et al. 1987; Boothroyd & Sackmann 1999). Therefore it is important to quantitatively know the uncertainties arising from nucleosynthesis in order to help constrain mixing processes using observations. In addition, the oxygen isotope predictions are important for the interpretation of pre-solar corundum (Al_2O_3) from meteorites for which oxygen isotopic ratios can be measured with high precision (e.g. Huss et al. 1994; Nittler et al. 1997).

During the main sequence (MS) evolution of low- and intermediate-mass stars, partial H-burning in the envelope produces ^{17}O , ^{13}C , and ^{14}N while ^{12}C , ^{15}N , and ^{18}O are destroyed (Fig. 1). The abundance of ^{16}O in the envelope is essentially unchanged for stellar mass $\leq 1.5 M_\odot$. For more massive stars, core convection on the early MS reaches out to ~ 25 per cent of the stellar mass, leaving behind core processed material as it retreats, including de-

* E-mail: fherwig@uvastro.phys.uvic.ca

stroyed ^{16}O (e.g. Schaller, Schaerer, Meynet, & Maeder 1992). Evidence of the retreating core convection is seen in the 2 and 3 M_{\odot} cases in Fig. 1 at the bottom of the envelope where the H and ^{16}O are depleted.

At the end of the MS phase hydrogen is exhausted in the core, causing the core to contract and the envelope to expand and cool. Envelope convection descends into the star as the envelope temperature drops. Regions previously affected by cool H-burning are homogenised, leading to a change of surface abundances (1st dredge-up, 1dup hereafter). As a result of this mixing, theory predicts the $^{16}\text{O}/^{17}\text{O}$ ratio decrease from initially ~ 2600 to a few hundred, depending on stellar mass while the $^{16}\text{O}/^{18}\text{O}$ ratio increases only marginally by ≤ 20 per cent from the initial value of about 500, weakly dependent on mass. For many stars, this is in fair agreement with spectroscopic observations. For example, Harris & Lambert (1984) find for K-giants $^{16}\text{O}/^{17}\text{O}$ ratios in the range 300 . . . 1000 and $^{16}\text{O}/^{18}\text{O} \sim 425 . . . 600$. Similarly, some corundum oxygen isotopes are in rough agreement with standard 1dup model predictions (e.g. SEAL203 in Choi, Huss, & Wasserburg (1998) has $^{16}\text{O}/^{17}\text{O} = 355$ and a solar $^{16}\text{O}/^{18}\text{O}$ ratio) while many others require either non-solar initial $^{16}\text{O}/^{18}\text{O}$ ratios (Huss et. al. 1994; Boothroyd, Sackmann, & Wasserburg 1994; Timmes, Woosley, & Weaver 1995) or non-standard mixing processes.

The dependence of oxygen isotopic ratios on the ^{17}O proton capture nuclear reactions has been studied before by El Eid (1994) and Boothroyd, Sackmann, & Wasserburg (1994). They considered the effect of a new determination of these reactions by Landre et al. (1989) and found that the uncertainty of the $^{16}\text{O}/^{17}\text{O}$ predictions is dominated by the uncertainty of these rates for stars with initial masses larger than $\sim 2.5M_{\odot}$.

In this paper we include seven reactions in a systematic analysis of the influence of rate uncertainties on the predicted oxygen isotopic ratios in red giant branch (RGB) stars. In addition to addressing this scientific question, we also want to demonstrate and test the method of evaluating model error propagation described here. Sect. 2 describes the method and computations. In Sect. 3 the uncertainty in the modeled oxygen isotopic ratios of RGB stars is analysed for significant reaction rate uncertainties and comparisons are made to observations and other models. A summary is in the final section.

2 METHOD AND MODELS

The nucleosynthesis and mixing considered here do not alter the structural evolution. Therefore we can efficiently post-process a time sequence of full stellar models to analyse the behaviour of nucleosynthesis and mixing in the envelope under variations of the input nuclear reaction rates. A sequence is post-processed many times, each time with a different set of values for the reaction rates (within published uncertainty) to obtain a Monte Carlo (MC) estimate of error propagation into the surface abundance predictions. In the following subsections we describe the stages of this method in more detail.

2.1 Evolution code

A time sequence of stellar models is generated by the *EVOL* code (see Herwig 2000; Blöcker 1995, and references therein). At each time step the four partial differential equations of stellar structure are solved on a 1D Lagrangian grid, with the *OPAL* opacity tables from Iglesias & Rogers (1996). A standard nuclear reaction

network, including the PP-chains and the CNO tri-cycle, is incorporated.

The treatment of mixing, in particular the use of convective overshooting, is not essential to this study because we are interested here in the differential impact of the uncertainties of nuclear reaction rates. However, there is some agreement that the hydrodynamical properties of convection inevitably result in some turbulent mixing into the neighboring stable layers, defined by the convective boundary where the acceleration of streams disappears. Models of convection in the hydrodynamical framework predict that the turbulent velocity field decays roughly exponentially (e.g. Xiong 1985; Freytag, Ludwig, & Steffen 1996; Asida & Arnett 2000). However, the extent of overshooting is not the same at all convective boundaries. This is evident from hydrodynamical simulations, for example by Freytag, Ludwig, & Steffen (1996) who find $f_{ov} = 0.25$ for the shallow surface convection of A-stars and $f_{ov} = 1.0$ for white dwarfs. Herwig, Bloeker, Schoenberner, & El Eid (1997) found that $f_{ov} = 0.02$ reproduces the results of Schaller, Schaerer, Meynet, & Maeder (1992) who fitted the observed width of the main sequence with an instantaneous treatment of overshooting of $0.2H_p$. This order of magnitude for core convection overshooting was confirmed by 2D hydrodynamical models by Deupree (2000). For a situation with an extended, deep envelope, like during the first dredge-up, an estimate of overshooting efficiency is more difficult. Alongi, Bertelli, Bressan, & Chiosi (1991) found that the position of the RGB luminosity bump can be aligned with observation with an envelope overshooting three times the value required for the core overshooting (see, however, Cassisi & Salaris 1997). Blöcker et al. (1998) found that overshooting at the bottom of the solar convection zone in excess of $f_{ov} = 0.07$ would cause too much lithium destruction (see also Schlattl & Weiss 1999). In view of the ambiguous evidence we decided to use the same value as for the main sequence core convection at the bottom of the descending envelope convection during the first dredge-up evolution.

For the core convection we use no overshooting in the 1 M_{\odot} cases, $f_{ov} = 0.008$ in the 1.5 M_{\odot} sequence and $f_{ov} = 0.016$ for the 2 M_{\odot} and 3 M_{\odot} cases. The mixing efficiency in the envelope is chosen to be $f_{env} = 0.016$ for all cases. The Reimer's mass loss formulae (Reimers 1975) with $\eta = 0.5$ for $M < 1.7 M_{\odot}$ and $\eta = 1.0$ for $M > 1.7 M_{\odot}$ is employed, starting at the bottom of the RGB.

2.2 Post-processing code and the Monte Carlo Scheme

Our post-processing code takes the stellar structure from the full stellar evolution model sequences generated by *EVOL* as input and recomputes abundance changes due to nucleosynthesis and mixing. The code is fully implicit, iterative, and couples mixing with nucleosynthesis using adaptive step size and full error control.

All reactions in the post-processing code use NACRE reaction rates (Angulo et al. 1999), which include estimates on upper and lower limits. We have used the electronic web tool *Netgen* (Jorissen & Goriely 2001) to retrieve the tabulated rates. The full network of nuclear reactions is the same as in the full stellar evolution code, but rates for a predefined set of seven reactions were systematically altered.

If one is interested in knowing the abundance uncertainty of a particular species, then inspection of its production and destruction reactions may reveal to which reaction uncertainty the abundance is most sensitive. For example, ^{18}O is mainly destroyed rather than produced in the envelope. Hence, the surface abundance of ^{18}O after 1dup ought to be most sensitive to the one of the two major

reactions which consume it. Reaction $^{18}\text{O}(p, \alpha)^{15}\text{N}$ has a larger nominal rate than $^{18}\text{O}(p, \gamma)^{19}\text{F}$ and accordingly this reaction must be most important to ^{18}O . While such a qualitative consideration is straightforward it is harder to estimate the quantitative effect of the uncertainty of this reaction because the combined effects of $^{18}\text{O}(p, \alpha)$ and the other reactions when the temperature profile evolves before equilibrium is reached and core convection on the early main sequence may affect the envelope abundances.

Manipulating the rates of one reaction that is part of a larger network will not necessarily reveal the whole picture, especially when equilibrium abundances are not achieved. This is true in particular for a general network situation in which reaction flows may be redirected due to uncertainties of reactions that are involved in branchings. In order to have a tool available which can readily be applied to any nucleosynthesis and mixing scenario we decided to take a general and flexible approach by combining post-process calculations with an MC scheme, as described below. With this approach we could, for example, also study more complex situations like the dependence of the *s*-process in asymptotic giant branch (AGB) stars on nuclear reaction rate uncertainties.

For each MC iteration the reaction rate for reaction *x* is given by

$$R_i^x(T) = \xi_i^x (R_u^x(T) - R_n^x(T)) + R_n^x(T), \quad 1 \geq \xi_i^x \geq 0 \quad (1)$$

$$R_i^x(T) = \xi_i^x (R_n^x(T) - R_l^x(T)) + R_n^x(T), \quad 0 > \xi_i^x \geq -1 \quad (2)$$

where $1 \geq \xi_i^x \geq -1$, and R_u^x , R_n^x , R_l^x are the upper, nominal, and lower rates respectively. We choose a Gaussian distribution to the random variable ξ_i which peaks at zero and has an e-folding distance at $\xi_i = .55$ so that the extreme values are populated at 1.8σ . Note that while the distribution on ξ_i is symmetric, the distribution of $R(T)$ is not.

2.3 Details of the computed models

With the stellar evolution code we generated seven sequences of stellar structure models for a range of initial mass and metallicity. Each sequence was followed from the beginning of the MS to just after the end of the 1dup. The stellar model sequences together with the mass coordinate of the deepest penetration of the 1dup (M_{dup}) and the maximum temperature achieved at that mass coordinate are listed in Table 1. The maximum envelope temperature was achieved at about $\frac{4}{5}$ of the MS lifetime for all cases. The envelopes of the 2–3 M_{\odot} cases receive matter from the core due to core convection on the early MS. For these cases, Table 1 also shows the maximum temperature achieved at the centre of the star (T_c) from the beginning of the MS to when the core convection no longer overlaps with the envelope. These temperatures are the maximum that part of the surface material, after 1dup, was exposed to.

Out of the full stellar evolution model sequences about 32 to 36 models for 1–1.5 M_{\odot} cases and 82 to 119 models for 2–3 M_{\odot} were chosen for post-processing. The bulk of extra models used in the 2–3 M_{\odot} cases were put on the first half of the MS, when core convection was retreating, leaving behind material processed in the core. At least 4 models were put near the time of deepest 1dup to ensure that a precise mixing depth was achieved. We post-processed the whole star for 2–3 M_{\odot} but only the envelope layers affected by the 1dup for 1–1.5 M_{\odot} . In this study we ignore any extra mixing processes that might occur later on the RGB, like cool bottom processing (Wasserburg, Boothroyd, & Sackmann 1995). The choice of stellar cases spans 1 M_{\odot} to 3 M_{\odot} with solar metallicity and additional cases for 1 M_{\odot} and 2 M_{\odot} where the metallic-

ity is lower. For the lower metallicity cases we have scaled all three oxygen isotopes with *Z*, *not* taking into account the anti-correlation of the $^{16}\text{O}/^{18}\text{O}$ with *Z* reported by Timmes, Woosley, & Weaver (1995). To facilitate comparison, the initial oxygen isotope ratios were chosen to be $^{16}\text{O}/^{17}\text{O}_i = 2465$ and $^{16}\text{O}/^{18}\text{O}_i = 442$, the same as in El Eid (1994).

Fig. 1 shows example abundance profiles produced by the post-processing code using the nominal reaction rates, together with the 1dup mark. One can see that ^{17}O is particularly sensitive to the maximum depth of the 1dup for the 1 M_{\odot} and 1.5 M_{\odot} cases because of the sharp rise in ^{17}O at the bottom of the 1dup (Landre et al. 1990). The reduced ^{16}O at the bottom of the envelope, from where core convection retreated, enhances the sensitivity to the maximum depth of the 1dup for the 2 M_{\odot} and 3 M_{\odot} cases.

The seven CNO cycle reactions which are included in the analysis are listed in Table 2 in decreasing order of $R_n(\log T = 7)$. The reaction $^{16}\text{O}(p, \gamma)^{17}\text{F}$ is followed by a rapid β^+ decay and draws from a large reservoir of ^{16}O to produce ^{17}O . Reaction $^{17}\text{O}(p, \gamma)^{18}\text{F}$ consumes ^{17}O to produce ^{18}O . Branching off from this series are reactions $^{18}\text{O}(p, \alpha)^{15}\text{N}$ and $^{18}\text{O}(p, \gamma)^{19}\text{F}$, which consume ^{18}O , and $^{17}\text{O}(p, \alpha)^{14}\text{N}$, which consumes ^{17}O . For the 1 M_{\odot} cases, reaction $^{16}\text{O}(p, \gamma)^{17}\text{F}$ is slow enough and ^{16}O is abundant enough that the ^{16}O reservoir is effectively not changing in the envelope. This is not true for 2–3 M_{\odot} (see Fig. 1), and therefore reactions $^{15}\text{N}(p, \gamma)^{16}\text{O}$ and $^{19}\text{F}(p, \alpha)^{16}\text{O}$ should receive attention in these cases because they affect the production of ^{16}O . Fig. 2 shows the nominal, upper and lower limits on these reaction rates for the relevant temperature range.

3 RESULTS

The primary result from the MC simulations are quantified model uncertainties in the oxygen isotopic ratios due to reaction rate uncertainties. Secondly, we assess the individual contribution from each of the considered reaction uncertainties on isotopic ratio uncertainties.

An MC simulation was carried out for each of the cases in Table 1 and the results are summarized in Table 3 and Fig. 8. The isotopic ratio uncertainties are derived from the distribution of points in triple isotope plots. The upper error bars for $^{16}\text{O}/^{18}\text{O}$ are defined to be the location of a horizontal line separates 2 per cent of the points above the line, and 98 per cent of the points are below. The lower error bar is where 98 per cent are above and 2 per cent are below. Error bars for $^{16}\text{O}/^{17}\text{O}$ are defined similarly. Therefore, the total number of MC points that lie outside of the error bars is ≤ 8 per cent. This scheme helps ensure that the errors bars are nearly invariant to the number of iterations. There were 200 iterations for each 1–1.5 M_{\odot} case, and at least 400 iterations for each $> 1.5 M_{\odot}$ case, which are already more time consuming due to a greater number of input models. More iterations are needed for the $> 1.5 M_{\odot}$ cases because there are 3 instead of 2 influential reaction rate uncertainties.

3.1 The triple isotope plots from the MC simulation

Fig. 3 shows a typical result from an MC simulation. Each point on the triple oxygen isotope plot represents the isotopic ratios after the 1dup for one iteration. The set of ξ_i^x for each iteration allows one to locate points with reaction rates far from the nominal value. In Fig. 3 a symbol associated with reaction *x* is over-plotted

if $|\xi_x^x| > 0.7$ (i.e. $> 1.4\sigma$) is satisfied for that reaction. Multiple symbols may be over-plotted for individual iterations. In this way the oxygen isotopic ratios from iterations for which reaction x was near an upper or lower limit are flagged. The distribution of the flagged iterations can reveal the relative importance of the uncertainties of the reactions considered. Symbols for reactions that do not dominate the isotopic uncertainties can appear everywhere in the cloud of points, indicating that a rate far from the nominal value for these reactions does not cause any preferred location in the plot (reaction $^{15}\text{N}(p, \gamma)^{16}\text{O}$ for example). The lack of symbols from reaction $^{18}\text{O}(p, \alpha)^{15}\text{N}$ in a horizontal band through the central region of the plot indicates that its reaction rate uncertainty overwhelmingly dominates the others in affecting the $^{16}\text{O}/^{18}\text{O}$ error. Reaction $^{18}\text{O}(p, \alpha)^{15}\text{N}$ causes scatter on the ordinate because it destroys ^{18}O . Fig. 6 shows this more clearly.

For the $3 M_{\odot}$ case shown, reactions $^{16}\text{O}(p, \gamma)^{17}\text{F}$ and $^{17}\text{O}(p, \alpha)^{14}\text{N}$ are responsible for the scatter on the abscissa because they most strongly affect ^{17}O . This fact is not clear from Fig. 6 because neither one clearly dominates. With random ξ_i there are many iterations where there is a cancelling effect, leading to points in the middle part of the cloud. In order to demonstrate this we do 15 separate runs of the post-processing code. In the first run, all rates are held at nominal. In the subsequent 14 runs, each of the 7 reaction rates takes its upper, then lower value while the other rates remain at the nominal value. The result of the 15 runs is illustrated in Fig. 4 for the $3 M_{\odot}$ case. Reaction $^{17}\text{O}(p, \alpha)^{14}\text{N}$ affects the abscissa and reaction $^{16}\text{O}(p, \gamma)^{17}\text{F}$ affects the ordinate secondly, but primarily affects the abscissa, as one might expect from inspection of the CNO network. Fig. 5 shows a similar 15 combination run on the $1.5 M_{\odot}$ case. For masses $\leq 1.5 M_{\odot}$ the envelope does not receive matter processed in the core, and hence the surface abundances are a product of nuclear processing at cooler temperatures. As a result, uncertainty of the $^{17}\text{O}(p, \alpha)^{14}\text{N}$ reaction loses all of its effect on $^{16}\text{O}/^{17}\text{O}$ uncertainty for stellar mass $\leq 1.5 M_{\odot}$ cases. Fig. 7 shows the absence of points in the centre for the dominant reactions.

The point distribution in the MC triple isotope plots of course depends on the choice of the e-folding distance for the random variable ξ_i . The distributions typically have patterns due to the asymmetric nature of reaction rate uncertainties. For example the bimodal distribution in Fig. 6 (high point density in the lower half and low density for larger $^{16}\text{O}/^{18}\text{O}$) is a consequence of the large upper limit for reaction $^{18}\text{O}(p, \alpha)^{15}\text{N}$.

3.2 Discussion of reaction uncertainties

Reaction $^{16}\text{O}(p, \gamma)^{17}\text{F}$ has a relatively low uncertainty (Fig. 2). For example at $\log T = 7.4$ the upper and lower limit according to the NACRE compilation are ± 30 per cent. This reaction derives its effect from the large (virtually constant) reservoir of ^{16}O which leads to a strong production rate of ^{17}O . Although the reaction rate of $^{17}\text{O}(p, \alpha)^{14}\text{N}$ is about two times greater than that of $^{16}\text{O}(p, \gamma)^{17}\text{F}$, ^{17}O is produced because the abundance of ^{16}O is about 3000 times greater than that of ^{17}O . Hence, the uncertainty in reaction $^{16}\text{O}(p, \gamma)^{17}\text{F}$ is more important to the surface abundance of ^{17}O .¹ In the past, reaction rates for $^{17}\text{O}(p, \alpha)^{14}\text{N}$ and $^{17}\text{O}(p, \gamma)^{18}\text{F}$ were very uncertain (see Sect. 3.2 El Eid 1994). With the modern, smaller NACRE uncertainty, uncertainty in reaction

$^{17}\text{O}(p, \alpha)^{14}\text{N}$ is still relevant to the $^{17}\text{O}/^{16}\text{O}$ 1dup predictions for the $2\text{--}3 M_{\odot}$ cases. Modern uncertainty in reaction $^{17}\text{O}(p, \gamma)^{18}\text{F}$, however, is not significant in the cases studied here.

For the $2\text{--}3 M_{\odot}$ cases, reactions $^{17}\text{O}(p, \alpha)^{14}\text{N}$ and $^{16}\text{O}(p, \gamma)^{17}\text{F}$ (starred triangles and triangles respectively in Fig. 4) have a similar influence on $^{16}\text{O}/^{17}\text{O}$. In the $2\text{--}3 M_{\odot}$ cases the combined effect of the uncertainty in these two reaction rates can cooperate to give some extreme $^{16}\text{O}/^{17}\text{O}$ values as well as partially cancel to give points in the central part of the cloud.

Reaction $^{18}\text{O}(p, \alpha)^{15}\text{N}$ strongly effects the isotopic abundances because its uncertainty is very large at the envelope temperatures of these stellar cases. Also note that reaction $^{18}\text{O}(p, \gamma)^{19}\text{F}$ has no noticeable effect on ^{18}O . Even though the error for this reaction is very large, reaction $^{18}\text{O}(p, \alpha)^{15}\text{N}$ is faster and therefore more important to the destruction of ^{18}O .

The effect of stellar mass and metallicity on the isotope ratio uncertainties is detectable mostly in $^{16}\text{O}/^{17}\text{O}$. The $^{16}\text{O}/^{18}\text{O}$ uncertainty is typically $+20/-5$ per cent due to reaction $^{18}\text{O}(p, \alpha)^{15}\text{N}$. For cases $> 1.5 M_{\odot}$, with higher temperatures ($2 M_{\odot}$, $Z=0.001$ and $3 M_{\odot}$, $Z=0.02$ especially) greater ^{16}O destruction and ^{17}O production can be seen at the surface. Hence, the destruction rate of ^{17}O rivals its production from ^{16}O , so the effect of uncertainty in reaction $^{17}\text{O}(p, \alpha)^{14}\text{N}$ is visible at the surface.

The interaction between the core and envelope convection for the $> 1.5 M_{\odot}$ cases means different temperature environments are seen by some of the dredged up material, than are seen by the $\leq 1.5 M_{\odot}$ cases. This adds to the complexity and has a very noticeable impact on the propagation of reaction rate uncertainty to surface abundances because it means uncertainties at a wider variety of temperatures become important.

3.3 Comparison with observations and other models

Our isotopic ratios, with the nominal rates, agree with results from Boothroyd, Sackmann, & Wasserburg (1994) that predict a strong dependence of $^{16}\text{O}/^{17}\text{O}$ on stellar mass. With increasing stellar mass from $1 M_{\odot}$ to $2 M_{\odot}$, $^{16}\text{O}/^{17}\text{O}$ decreases from 2500 to 100 for $Z=0.02$ in Fig. 8 (i.e. ^{16}O destruction in the envelope increases for $> 1.5 M_{\odot}$ and the ^{17}O production is increased in all cases). Our predictions show increasing $^{16}\text{O}/^{17}\text{O}$ with increasing mass for the $> 2 M_{\odot}$ cases, producing a minimum at about $2 M_{\odot}$, the same as in El Eid (1994) (see also Boothroyd, Sackmann, & Wasserburg 1994). The inset in Fig. 8 shows model predictions by El Eid (1994) and this study (asterisks and filled boxes respectively) for $2 M_{\odot}$ and $3 M_{\odot}$. The difference between our $^{16}\text{O}/^{17}\text{O}$ predictions and those of El Eid (1994) is partially explained by our different choice for the important $^{17}\text{O}(p, \alpha)^{14}\text{N}$ reaction rate. The lower limit on this rate, used in this study, is similar to the rate used to predict the asterisks. Uncertainty in the treatment of mixing processes, which is not propagated with the MC simulations, likely makes the largest contribution to the difference.

The dependence of oxygen abundance ratios on stellar metallicity is tied to dependence of structure (temperature) to metallicity. The predicted ratios for the two $1 M_{\odot}$ cases are indistinguishable given the calculated uncertainty. The predictions for three $2 M_{\odot}$ cases are distinguishable. Lower metallicity produces higher temperatures and greater overall ^{18}O destruction, causing higher $^{16}\text{O}/^{18}\text{O}$ for those cases.

Spectroscopic observations of the isotope ratios in RGB stars from Harris & Lambert (1984); Harris, Lambert, & Smith (1988) are also shown in Fig. 8 and Table 4. These stars are either ascending the RGB for the first time or are undergoing core He-burning

¹ Production (or destruction) rate is $r = N_a N_b \langle \sigma v \rangle$, where N_a and N_b are the molar densities of the reactants and $\langle \sigma v \rangle = R$ is the reaction rate.

on the blue loops. Hence, the surface abundances of these stars have been changed by the 1dup. The mass- $^{16}\text{O}/^{17}\text{O}$ relationship is roughly obeyed by these observations (see El Eid 1994, for a discussion).

The prediction band in Fig. 8 was from an initial $^{16}\text{O}/^{18}\text{O}$ which is 10 per cent smaller than the solar value, giving predictions that overlap with all but one of the spectroscopic observations. However, the number of post-1dup observations below solar ($^{16}\text{O}/^{18}\text{O}=498$) and below the band predicted from initial $^{16}\text{O}/^{18}\text{O}=442$ is worth noticing. When there is a slight shift in the initial oxygen isotopic ratios, there is a proportional shift in the modeled post-1dup ratios (as shown by Boothroyd, Sackmann, & Wasserburg 1994). Hence, if the model prediction of about a 15 per cent increase in $^{16}\text{O}/^{18}\text{O}$ after 1dup is correct, then some of the stars with spectroscopic data in Fig. 8 (circles) must have had initial $^{16}\text{O}/^{18}\text{O}$ values ~ 30 per cent less than solar (super-solar metallicity). In addition, the post-1dup spectroscopic data shown in Fig. 8 roughly correlate with $[\text{Fe}/\text{H}]$ measurements compiled by Taylor (1999) (Table 4), but indicate a pre-solar metallicity. There is currently no reason to believe that ^{18}O is not depleted in the envelope during the MS. A possible explanation is additional mixing above the core that further depletes ^{16}O in the envelope, leading to an decreased $^{16}\text{O}/^{18}\text{O}$ after 1dup. Testing this hypothesis will be appropriate when more precise spectroscopic observations become available.

Pre-solar meteoritic inclusions have been linked to giant stars due to their specific isotopic abundance signatures (Huss et al. 1994; Zinner 1998). The rather large spread of their oxygen isotopic ratios implies additional mechanisms at work (like initial isotope ratio variations or extra mixing processes). The variations of isotope ratios in grains are much larger than the model uncertainties due to nuclear reaction rates. However, better nuclear data would be required to improve the identification of these extra mechanisms.

4 CONCLUSIONS

In this paper we quantify the uncertainty in oxygen isotopic ratios due to uncertain reaction rates. These results may help to motivate and prioritize new laboratory measurements of reaction rates. Reaction rate uncertainty for $^{16}\text{O}(\text{p}, \gamma)^{17}\text{F}$ and $^{18}\text{O}(\text{p}, \alpha)^{15}\text{N}$ are significant to oxygen isotope ratios for all of the stellar cases studied here. Reaction $^{17}\text{O}(\text{p}, \alpha)^{14}\text{N}$ competes with $^{16}\text{O}(\text{p}, \gamma)^{17}\text{F}$ for dominance in $^{16}\text{O}/^{17}\text{O}$ uncertainty for the 2–3 M_{\odot} cases because of the interaction between core mixing and subsequent envelope mixing. Of course, this result is based on the assumption that the estimated uncertainties in the reaction rates (NACRE upper and lower limits) are appropriate.

In general, reactions with large uncertainties, and reactions with slow reaction rates but large production/destruction rates and *any* uncertainty create the largest uncertainty in isotopic ratios. The MC scheme demonstrated here efficiently finds the most problematic rates and provides a means of quantifying uncertainties for a particular stellar environment.

The model uncertainties calculated here are from reaction rate uncertainties only. The total model uncertainty in oxygen isotopic ratios definitely has contributions from uncertainty in mixing processes. This problem will become more tractable as the uncertainties due to reaction rates are made smaller.

ACKNOWLEDGMENTS

J. S. is grateful for support from the Herzberg Institute for Astrophysics, a division of the National Research Council of Canada. F. H. appreciates support from Dr. D. A. Vandenberg through his Operating Grant from the Natural Science and Engineering Research Council of Canada. F. H. thanks Dr. A. C. Shotton for his interest in this work and the hospitality at TRIUMF, Vancouver, BC. F. H. would also like to thank Dr. C. Iliadis for stimulating discussions and his hospitality at TUNL, Durham, NC.

REFERENCES

- Alongi, M., Bertelli, G., Bressan, A., & Chiosi, C. 1991, *A&A*, 244, 95
- Anders, E. & Grevesse, N. 1989, *Geochimica et Cosmochimica Acta*, 53, 197
- Angulo, C. et al. 1999, *Nuclear Physics A*, 656, 3
- Asida, S. M. & Arnett, D. 2000, *ApJ*, 545, 435.
- Bloecker, T. 1995, *A&A*, 297, 727
- Blöcker, T., Holweger, H., Freytag, B., Herwig, F., Ludwig, H.-G., & Steffen, M. 1998, *Space Science Reviews*, 85, 105
- Boothroyd, A. I., Sackmann, I.-J., & Wasserburg, G. J. 1994, *ApJL*, 430, L77
- Boothroyd, A. I. & Sackmann, I.-J. 1999, *ApJ*, 510, 232
- Cassisi, S. & Salaris, M. 1997, *MNRAS*, 285, 593
- Choi, B.-G., Huss, G. R., & Wasserburg, G. J. 1998, *Meteoritics & Planetary Science*, vol. 32, p. A32, 33, 32
- Deupree, R. G. 2000, *ApJ*, 543, 395
- El Eid, M. F. 1994, *A&A*, 285, 915.
- Freytag, B., Ludwig, H.-G., & Steffen, M. 1996, *A&A*, 313, 497
- Iglesias, C. A. & Rogers, F. J. 1996, *ApJ*, 464, 943
- Jorissen, A. & Goriely, S. 2001, *Nuclear Physics A* 688, 2001, p. 508c
- Harris, M. J. & Lambert, D. L. 1984, *ApJ*, 285, 674
- Harris, M. J., Lambert, D. L., & Smith, V. V. 1985, *ApJ*, 299, 375
- Harris, M. J., Lambert, D. L., Hinkle, K. H., Gustafsson, B., & Eriksson, K. 1987, *ApJ*, 316, 294
- Harris, M. J., Lambert, D. L., & Smith, V. V. 1988, *ApJ*, 325, 768
- Herwig, F. 2000, *A&A*, 360, 952.
- Herwig, F., Bloecker, T., Schoenberner, D., & El Eid, M. 1997, *A&A*, 324, L81
- Huss, G. R., Fahey, A. J., Gallino, R., & Wasserburg, G. J. 1994, *ApJL*, 430, L81.
- Landre, V., Aguer, P., Bogaert, G., Lefebvre, A., Thibaud, J. P., Fortier, S., Maison, J. M., & Vernotte, J. 1989, *Phys. Review C*, 40, 1972
- Landre, V., Prantzos, N., Aguer, P., Bogaert, G., Lefebvre, A., & Thibaud, J. P. 1990, *A&A*, 240, 85
- Nittler, L. R., Alexander, C. M. O., Gao, X., Walker, R. M., & Zinner, E. 1997, *ApJ*, 483, 475
- Reimers, D. 1975, *Problems in stellar atmospheres and envelopes*. (A75-42151 21-90) New York, Springer-Verlag New York, Inc., 1975, p. 229-256., 229
- Schlattl, H. & Weiss, A. 1999, *A&A*, 347, 272
- Schaller, G., Schaerer, D., Meynet, G., & Maeder, A. 1992, *A&AS*, 96, 269
- Taylor, B. J. 1999, *A&AS*, 139, 63
- Timmes, F. X., Woosley, S. E., & Weaver, T. A. 1995, *ApJS*, 98, 617
- Wasserburg, G. J., Boothroyd, A. I., & Sackmann, I.-J. 1995, *ApJL*, 447, L37

Xiong, D. R. 1985, *A&A*, 150, 133

Zinner, E. 1998, *Annual Review of Earth and Planetary Sciences*,
26, 147

Table 1. The seven different stellar cases considered with the maximum temperature achieved in the envelope during the MS. The mass coordinate of the deepest penetration of the 1dup is M_{dup} and T_c is the central temperature.

mass (M_{\odot})	metallicity	M_{dup} (M_{\odot})	max[log T(M_{dup})] (K)	max[log T_c] (K)
1.0	0.01	0.23	7.12	-
1.0	0.02	0.225	7.11	-
1.5	0.02	0.25	7.22	-
2.0	0.001	0.39	7.36	7.42
2.0	0.01	0.32	7.32	7.35
2.0	0.02	0.31	7.29	7.29
3.0	0.02	0.49	7.36	7.39

Table 2. Reactions included in the MC scheme, with nominal, lower and upper limits for reaction rates at $\log T = 7.0$ and $\log T = 7.4$.

reaction	log ($R_n(7.0)$) ($\text{sec}^{-1} \text{mol cm}^{-3}$)	log ($R_n(7.4)$) ($\text{sec}^{-1} \text{mol cm}^{-3}$)
$^{18}\text{O}(p, \alpha)^{15}\text{N}$	$-19.98^{+1.13}_{-0.70}$	$-11.81^{+0.30}_{-0.26}$
$^{15}\text{N}(p, \gamma)^{16}\text{O}$	$-20.36^{+0.07}_{-0.09}$	$-12.31^{+0.09}_{-0.12}$
$^{18}\text{O}(p, \gamma)^{19}\text{F}$	$-23.00^{+2.42}_{-0.78}$	$-14.89^{+0.17}_{-0.04}$
$^{19}\text{F}(p, \alpha)^{16}\text{O}$	$-23.75^{+0.12}_{-0.16}$	$-14.42^{+0.12}_{-0.16}$
$^{17}\text{O}(p, \alpha)^{14}\text{N}$	$-23.77^{+0.11}_{-0.15}$	$-13.66^{+0.09}_{-0.09}$
$^{17}\text{O}(p, \gamma)^{18}\text{F}$	$-24.17^{+0.08}_{-0.10}$	$-15.18^{+0.12}_{-0.12}$
$^{16}\text{O}(p, \gamma)^{17}\text{F}$	$-24.16^{+0.11}_{-0.15}$	$-15.41^{+0.11}_{-0.15}$

Table 3. The modeled surface oxygen isotopic ratios after 1dup, with errors from the MC simulations.

mass (M_{\odot})	metallicity, Z	$^{16}\text{O}/^{17}\text{O}$	$^{16}\text{O}/^{17}\text{O}$
1.0	0.01	2405^{+13}_{-17}	470^{+45}_{-13}
1.0	0.02	2410^{+13}_{-16}	469^{+46}_{-12}
1.5	0.02	1260^{+180}_{-130}	545^{+70}_{-20}
2.0	0.001	177^{+48}_{-25}	615^{+110}_{-30}
2.0	0.01	163^{+53}_{-22}	575^{+100}_{-28}
2.0	0.02	115^{+38}_{-20}	565^{+95}_{-20}
3.0	0.02	268^{+50}_{-32}	565^{+95}_{-20}
initial		2465	442

Table 4. Selected observations of oxygen isotope ratios. The first 8 are measured from spectroscopic observations of RGB stars. The two meteoric observations were extracted from individual dust grains that formed around AGB stars.

Object	mass ^a (M_{\odot})	$^{16}\text{O}/^{17}\text{O}$	$^{16}\text{O}/^{18}\text{O}$	ref ^b	[Fe/H] ^c
α Ari	1	520^{+100}_{-120}	450^{+40}_{-110}	1	-0.221
β Gem	1.3	240^{+50}_{-60}	510^{+90}_{-110}	1	-0.003
α Ser	1.4	300^{+150}_{-150}	400^{+200}_{-200}	1	+0.098
β UMi	1.5	510^{+70}_{-90}	440^{+70}_{-90}	1	-0.132
α Tau	1.5	600^{+150}_{-300}	475^{+125}_{-200}	2	-0.102
β Peg	1.7	1050^{+250}_{-500}	425^{+75}_{-150}	2	–
γ Dra	2	300^{+75}_{-150}	475^{+125}_{-200}	2	-0.178
μ Gem	2	325^{+75}_{-150}	475^{+125}_{-200}	2	–
β And	2.5	155^{+30}_{-50}	425^{+75}_{-150}	2	–
α UMa	3	330^{+50}_{-70}	600^{+125}_{-150}	1	-0.128
SEAL203	–	355	498	3	–
SEAL235	–	472	714	3	–
SEAL261	–	337	1190	3	–
solar	1	2622	498	4	0

^a Masses have an undetermined uncertainty.

^b Observations 1) at $5\mu m$ by Harris, Lambert, & Smith (1988) and 2) Harris & Lambert (1984), 3) meteoric observations by Choi, Huss, & Wasserburg (1998), 4) solar ratios by Anders & Grevesse (1989).

^c From Taylor (1999).

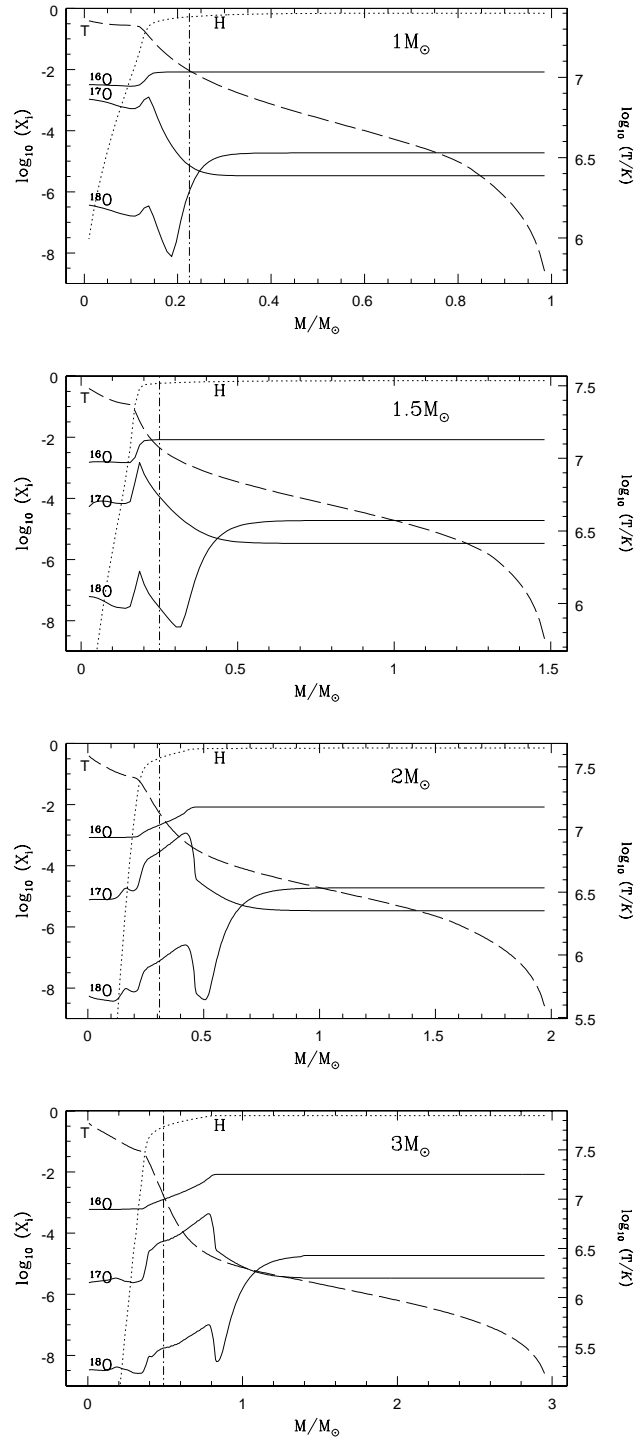


Figure 1. Mass fraction profiles of H (dotted), ^{16}O , ^{17}O , and ^{18}O (solid), as well as temperature (long dash) for the $1M_{\odot}$ (top left), $1.5M_{\odot}$ (top right), $2M_{\odot}$ (bottom left), and $3M_{\odot}$ (bottom right) cases with $Z=0.02$ near the end of the core H-burning. Also shown is the deepest penetration of the first dredge-up (dash-dot).

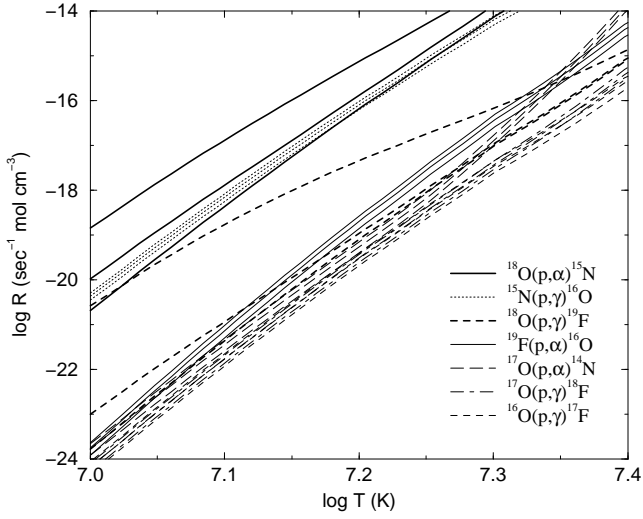


Figure 2. The nominal, upper and lower limits of the rates for the seven reactions. The order of reactions in the legend is the same as Table 2.

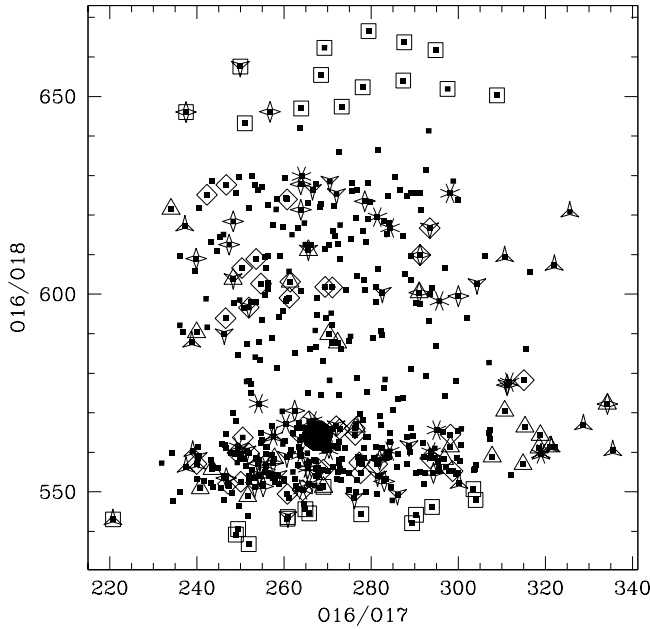


Figure 3. The surface oxygen isotope ratios for $3 M_{\odot}$ and $Z=0.02$ from an MC simulation with all seven reactions and 500 iterations. All points are plotted in small filled squares and over-plotted are points from iterations where $|\chi^2_i| > 0.7$ for each reaction; $^{15}\text{N}(p, \gamma)^{16}\text{O}$ (diamonds), $^{16}\text{O}(p, \gamma)^{17}\text{F}$ (open triangles), $^{17}\text{O}(p, \alpha)^{14}\text{N}$ (starred triangles up), $^{17}\text{O}(p, \gamma)^{18}\text{F}$ (asterisk), $^{18}\text{O}(p, \alpha)^{15}\text{N}$ (open squares), $^{18}\text{O}(p, \gamma)^{19}\text{F}$ (starred triangles down), $^{19}\text{F}(p, \alpha)^{16}\text{O}$ (starred diamonds). Note the lack of open triangles and squares in the centre (error dominant reactions $^{16}\text{O}(p, \gamma)^{17}\text{F}$ and $^{18}\text{O}(p, \alpha)^{15}\text{N}$).

This paper has been typeset from a $\text{\TeX}/\text{\LaTeX}$ file prepared by the author.

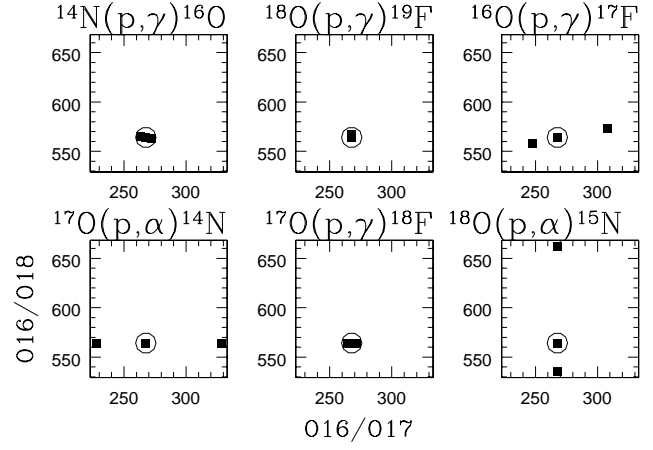


Figure 4. Oxygen isotope ratios for the $3 M_{\odot}$ $Z=0.02$ case when one reaction took the upper, lower, and nominal (circled) reaction rate while the other rates remained at nominal. Results from $^{19}\text{F}(p, \alpha)^{16}\text{O}$ (not shown) are the smallest.

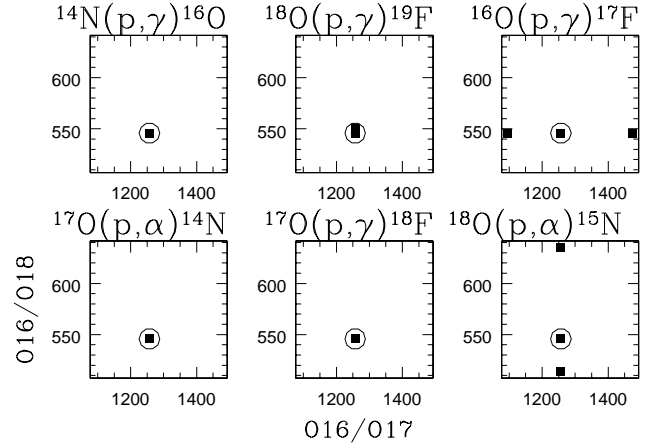


Figure 5. Same as Fig. 4, for the $1.5 M_{\odot}$ $Z=0.02$ case.

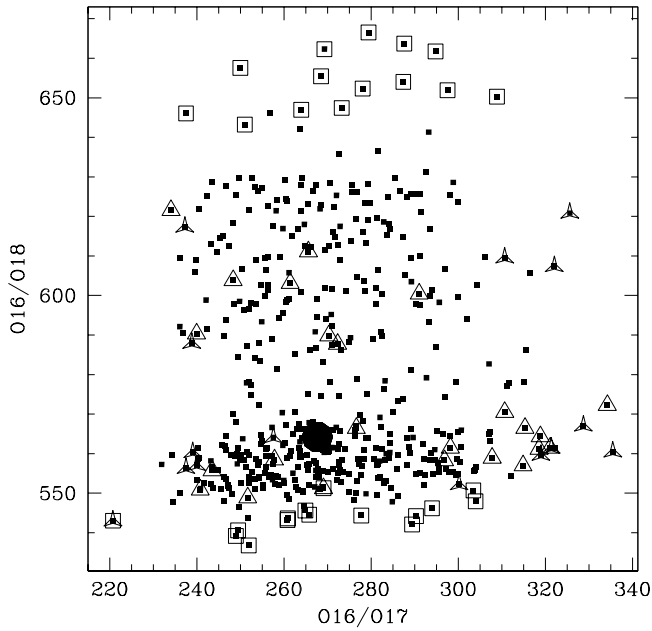


Figure 6. Same as Fig. 3 for the $3 M_{\odot}$ case, except only symbols from iterations where $|\xi_i^{16\text{O}(p,\gamma)^{17}\text{F}}| > 0.7$ (open triangles), $|\xi_i^{17\text{O}(p,\alpha)^{14}\text{N}}| > 0.7$ (starred triangles up), and $|\xi_i^{18\text{O}(p,\alpha)^{15}\text{N}}| > 0.7$ (open squares) are over plotted. A filled circle marks the point where the nominal rates were used for all reactions.

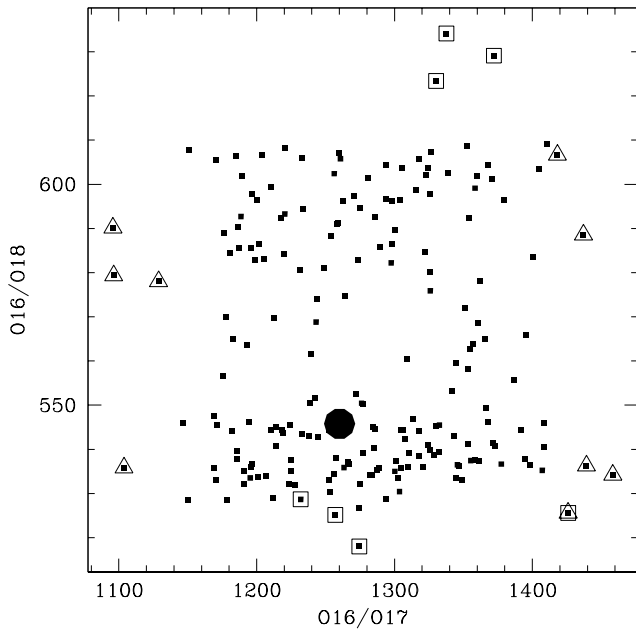


Figure 7. Same as Fig. 3 for the $1.5 M_{\odot}$ case with 200 iterations and only symbols from iterations where $|\xi_i^{16\text{O}(p,\gamma)^{17}\text{F}}| > 0.7$ (open triangles) and $|\xi_i^{18\text{O}(p,\alpha)^{15}\text{N}}| > 0.7$ (open squares) are over plotted. A filled circle marks the point where the nominal rates were used for all reactions.

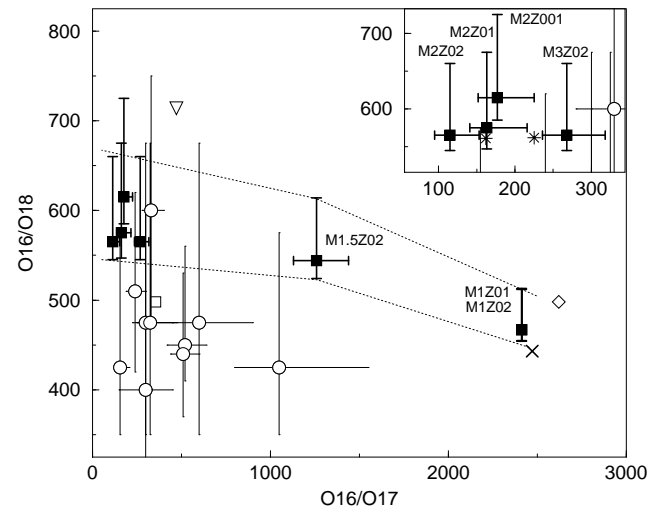


Figure 8. Modeled isotopic ratios with propagated errors derived from MC simulations for the seven stellar cases (filled squares, labeled with their mass and metallicity). The x marks the initial oxygen ratios before 1dup for all cases. Spectroscopic data (circles) from Harris & Lambert (1984); Harris, Lambert, & Smith (1988). Meteoric data from SEAL203 (open square), SEAL235 (open triangle) (Choi, Huss, & Wasserburg 1998), and solar (diamond). Dotted lines mark a band where $Z=0.02$ stars are predicted to exist with our choice of initial abundances. Inset shows our 2–3 M_{\odot} model predictions in more detail, as well as predictions of El Eid (1994) for $Z=0.02$, $2 M_{\odot}$ (left asterisk) and $3 M_{\odot}$ (right asterisk).